

Modeling of hyperelastic material accounting for the Mullins effect by defining a new stiffness reduction variable

Elisabeth Toups^{1*}, Robert Seewald², Benjamin Schaaf³, Hagen Holthusen¹, Uwe Reisgen², Markus Feldmann³, Stefanie Reese¹, and Jaan-Willem Simon¹

¹ RWTH Aachen University, Institute of Applied Mechanics, Mies-van-der-Rohe-Str. 1, 52074 Aachen, Germany

² RWTH Aachen University, Welding and Joining Institute, Pontstraße 49, 52062 Aachen, Germany

³ RWTH Aachen University, Institute of Steel Construction, Mies-van-der-Rohe-Str. 1, 52074 Aachen, Germany

Abstract: Supporting structures in the field of glass façade construction are increasingly relying on making use of silicone adhesives. Hence, predicting the hyperelastic behavior and the stiffness reduction (Mullins effect) of such adhesives is essential for the economical dimensioning of load-bearing bonds. For this, a phenomenological hyperelastic model at finite strains is defined, which enables an accurate prediction of the real material behavior. The presented model is based on the Ogden model. Two internal variables are defined, which describe stiffness reduction during loading and unloading procedures and hardening or softening behavior, to model the experimentally observed behavior. For the calibration of the corresponding material parameters, a staggered parameter identification scheme is proposed in order to obtain a unique parameter set for the representation of multiaxial stress states. The excellent model prediction is shown by selected examples.

Keywords: rubberlike material, hyperelasticity, Mullins effect, silicone adhesives, continuum damage mechanics, finite strains

1 Introduction

Load bearing bonds become increasingly common in glass-façade structures. This is due to their beneficial characteristics, such as the more continuous load transfer between glass and the supporting elements compared to alternative connections, and the possibility to achieve a more transparent design. Utilized adhesives show rubber-like, hyperelastic material response under large deformations. During experimental investigations, stiffness reduction is observed referred to as Mullins effect (see e.g. [Mullins \(1948\)](#), [Bueche \(1961\)](#)). Until now, German regulations for the dimensioning of load bearing bonds include very high safety factors ([ETAG \(2012\)](#)) which could be reduced by using a more sophisticated prediction of the real material behavior ([Richter et al. \(2014\)](#)). Thereby, a higher material utilization would be possible. To provide better predictions, a material model representing the complex behavior mentioned above is needed to enable a less time consuming and less cost intensive realistic calculation and design. To the phenomenological material models belong above all the classical approaches of [Mooney \(1940\)](#) and [Rivlin \(1948\)](#) as well as of [Ogden \(1984\)](#). These models are still frequently used today because they are relatively simple and contain only a small number of material constants to be characterized. Comparisons between these and other phenomenological models for the mechanical behavior of hyperelastic materials and the characterization of the associated parameters can be found in [Steinmann et al. \(2012\)](#), [Martins et al. \(2006\)](#), [Meunier et al. \(2008\)](#). There, it is shown that these models are suitable to describe the nonlinear elastic stress-strain behavior of rubber-like materials. However, these material models are not able to represent stress softening which occurs in the considered adhesives. This softening occurs particularly under repeated loading as is referred to as Mullins effect, which was first observed by [Bouasse and Carrière \(1903\)](#). In the last decades, a lot different approaches were figured out to model the Mullins effect. Ogden and Roxburgh proposed the idea that the model response of the material behavior can be described in terms of a pseudo-energy function. To describe the elastic behavior, an internal variable is set to a constant value and activated, so that damage occurs during relief ([Ogden and Roxburgh \(1999\)](#)). Dorfmann and Ogden developed a new approach based on the Ogden-Roxburgh model. They defined two variables within the free energy. The first variable describes the damage and softening behavior, the second variable describes the accumulation of residual strain during loading and unloading cycles and is called the residual strain variable ([Dorfmann and Ogden \(2004\)](#)). A more detailed overview of selected models describing the Mullins effect can be found in [Diani et al. \(2009\)](#). It is known from the literature that the stress strain behavior depends strongly on the angle between the current and the previous direction of loading. This anisotropy induced by the Mullins effect in the deformation history was already observed by e.g. [Mullins \(1948\)](#), [Arruda and Przybylo \(1995\)](#), [Pawelski et al., Besdo et al. \(2003\)](#). Studies on this topic can be found in e.g. [Ihlemann \(2005\)](#), [Itskov et al. \(2006\)](#), [Kahraman et al. \(2010\)](#).

This paper presents a phenomenological model to describe the softening (Mullins effect) of silicone adhesives based on the Ogden model with a thermodynamically consistent extension to account for the stiffness reduction, neglecting the above mentioned anisotropy and further effects like viscosity, hysteresis and plasticity. The model parameters are identified in a staggered procedure in such a way that a unique set of parameters is created which also enables the modeling of multi-axial stress states. Selected validation examples under consideration of multi-axial stress states are presented at the end.

* E-mail address: toups@ifam.rwth-aachen.de

2 Experimental studies and material behavior

To model the behavior of the silicone adhesive, at first, the experimental material behavior was observed. A uniaxial tension test was performed under cyclic loading up to a maximum technical strain of 100%. The experimental results were observed from that part of the specimen in between the white lines (see Fig. 1), where a homogeneous material behavior can be expected. The distance between these white lines is 20 mm and the dimensions of the test's relevant area, marked with the red box in Fig. 1 are 60 mm x 10 mm x 4 mm. The corresponding relation of logarithmic strain and first Piola Kirchhoff stress is shown in Fig. 1.

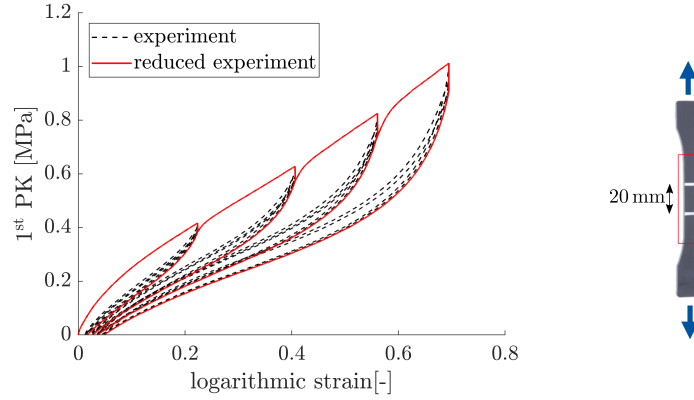


Fig. 1: Experimental observation: Uniaxial tension test

The stress strain behavior represents an S-shaped curve typical for hyperelastic materials. Furthermore, stiffness reduction can be observed, which is also described by the Mullins effect. The Mullins effect occurs during cyclic loading and in particular, the stress softening during the first and second loading and unloading cycles is noticeable. After about five to ten cycles, depending on the material, a stabilized hysteresis loop can be reached, see e.g. Harwood et al. (1965), Johnson and Beatty (1993), Beatty and Krishnaswamy (2000), Cantournet et al. (2009). There are different physical explanations and interpretations of the Mullins effect in literature. Rubbers in general consists of polymers. These polymer chains can be strengthened by adding particles, so that the filled rubber consists of a network of polymer chains filled with some particles Böhl (2005). The anisotropy induced by the Mullins effect, as observed e.g. by Mullins (1948), is neglected and in addition, no hysteresis effects, viscosity or plasticity are taken into account in the material model presented here. Therefore, the experimental data were reduced accordingly so that the idealized Mullins effect is preserved. For this the experimental data are read out in such a way that the load curves and the last relief curves per cycle are taken into account, the cycles in between are neglected. This is shown in Fig. 1 by the red curve. For the investigation of shear behavior, a pure shear test was studied. In a pure shear test, a special geometry of the specimen is required: One edge of the thin specimen must be much longer than the other. Investigations show that the dimension of the adhesive with 200 mm x 50 mm x 3 mm is suitable to generate a pure shear behavior within the considered adhesive. The pure shear behavior is observed in the center of the specimen. For illustration, the specimen in the loaded state due to elongation in y-direction, perpendicular to the longer edge length, is shown schematically in Fig. 2.

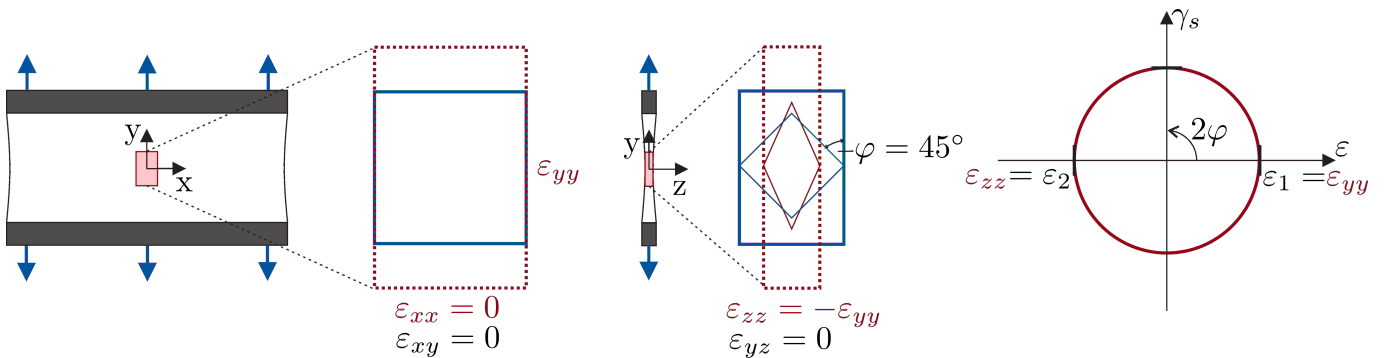


Fig. 2: Details about pure shear behavior in an incompressible material

Due to the chosen geometry there is no influence from the transversal contraction in the center of the specimen, so that $\epsilon_{xx} = 0$, and ϵ_{yy} increases because of the elongation. In contrast, ϵ_{zz} decreases due to the contraction in z-direction. Considering an incompressible material, the contraction in z-direction is equal to the elongation in y-direction, $\epsilon_{zz} = -\epsilon_{yy}$. This is indicated by the following deformation gradient:

$$F_{ij} = \begin{bmatrix} 1 & 0 & 0 \\ 0 & \lambda & 0 \\ 0 & 0 & \lambda^{-1} \end{bmatrix}, \quad (1)$$

where λ is the respective stretch. The plotted strains into y- and z-direction, which are exactly the same size, imply that a pure shear deformation is obtained at an angle of 90° in Mohr's circle. The maximum shear strain is reached when $\epsilon_{yy} = \epsilon_{zz} = 0$.

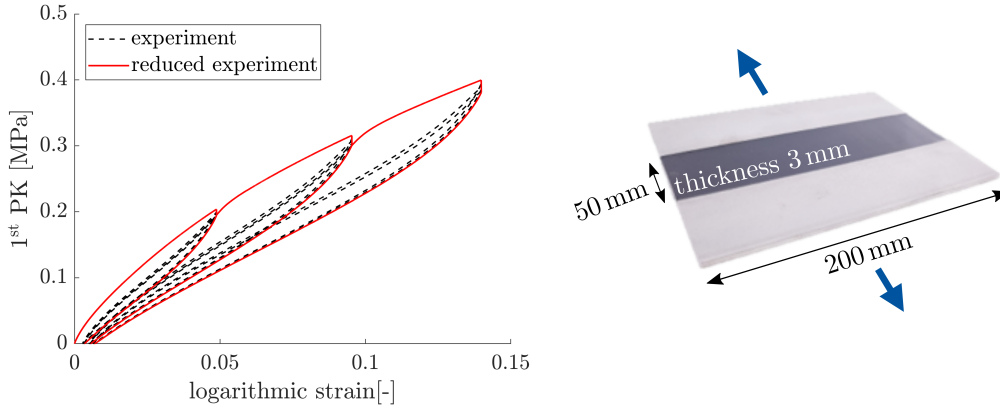


Fig. 3: Experimental observation: Pure shear test

In Fig. 3 the specimen used for the test procedure is shown. If the specimen constricts strongly due to its almost incompressible behavior at high strains, a pure sample may slip slightly out of the clamp each time a new strain level is approached. Joined specimens were used to avoid the remaining strain resulting from these friction losses in the clamping area. Stainless steel sheets were used as joining partners and clamped into the test bench. Since the stainless steel practically does not deform at the comparatively very low loads and thus does not change thickness, the problem of friction loss and the associated successive slippage of the specimen could be avoided. The load was thus transferred to the adhesive via adhesion to the parts to be joined and no longer via a frictional clamping effect. For evaluation, the logarithmic longitudinal strain perpendicular to the longer edge length and the first Piola Kirchhoff stress in the stretched direction are considered, see Fig. 3. Here, too, the curve obtained from the experiment is reduced to the envelope red curve.

At least a compression test was performed to investigate the volumetric deformation. Here, a cylindrical pure substance sample with a diameter of 20 mm and a height of 30 mm, is uniaxially loaded, while deformation in the other two spatial directions is prevented, see Fig. 4. A change in shape is only possible by reducing the volume. The experimental implementation takes place in a precisely fitting steel tube into which the test specimen is inserted and then loaded with a punching force. The nearly linear relation of pressure p and the specific volume ratio $\Delta V/V$ is shown in Fig. 4.

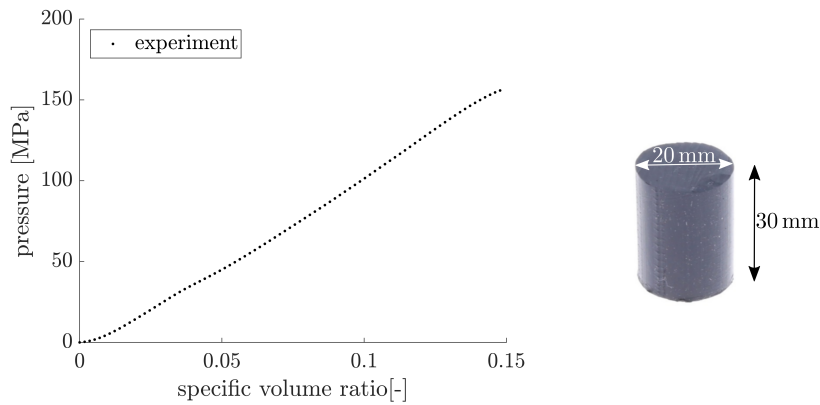


Fig. 4: Experimental observation: Compression test

3 Material modeling

The total Helmholtz free energy of this model is defined as

$$\psi = \psi_{el}(\lambda_1, \lambda_2, \lambda_3, \rho) + \psi_c(\delta), \tag{2}$$

where the first part is based on the Ogden model for hyperelasticity

$$\psi_{el}(\lambda_1, \lambda_2, \lambda_3, \rho) = \sum_{k=1}^3 \mu_k(\rho) \left[\frac{1}{\alpha_k} (\lambda_1^{\alpha_k} + \lambda_2^{\alpha_k} + \lambda_3^{\alpha_k} - 3) - \ln J \right] + \frac{\Lambda}{4} (J^2 - 1 - 2 \ln J), \tag{3}$$

the free energy function of which is defined as a function of the principal stretches λ_i , $i = 1, 2, 3$, and contains the material parameters μ_k and α_k . J is the product of the principal stretches and Λ is the Lamé constant. As a new variable ρ is defined for taking into account stiffness reduction. This variable is assumed to be a scalar and works as an internal variable taking values

between 0 and 1. The following formulation $\mu_k(\rho)$ is defined, which is used instead of the original parameters μ_k :

$$\mu_k(\rho) = \begin{cases} \mu_k^0 & \text{if } \rho = 0 \\ (1 - \rho)^{p_k} (\mu_k^0 - \mu_k^\infty) + \mu_k^\infty & \text{if } 0 < \rho < 1 \\ \mu_k^\infty & \text{if } \rho = 1 \end{cases} \quad (4)$$

In the standard continuum damage mechanics approach, the model response results in failure for the case $D = 1$ (D is the damage variable). On the contrary, in the current formulation, $\rho = 1$ does not refer to failure but to a final stress-strain relationship which can be represented by the model. The parameters μ_k^∞ are needed to describe this last stress-strain curve. In contrast, μ_k^0 (the value of $\mu_k(\rho = 0)$) are artificial parameters, which are needed to describe the stress-strain behavior during the stiffness reduction, and do not reflect any physical properties. The advantage of this embedded variable ρ is, that stiffness reduction is considered specifically in each Ogden term. The consideration of the newly introduced variable leads to an additional term ψ_c , which is added in the free energy function in order to control the development of stiffness reduction and to model the softening/hardening behavior (cf. e.g. [Brepols et al. \(2017\)](#), [Simon et al. \(2017\)](#)). For this control part, the following exponential formulation

$$\psi_c(\delta) = c_1 \left(\delta + c_2 e^{-\frac{\delta}{c_2}} - 1 \right) \quad (5)$$

was chosen, which depends on the softening/hardening variable δ and also contains the two model parameters $c_1 > 0$ and $c_2 > 0$. Both parts, $\mu_k(\rho)$ and $\psi_c(\delta)$, can be chosen freely and independently, making the model very flexible. Following general thermodynamical considerations, the second law of thermodynamics must be fulfilled and is therefore exploited to derive the state relations of the model.

$$-\dot{\psi} + \mathbf{P} \cdot \dot{\mathbf{F}} \geq 0 \quad (6)$$

$$\underbrace{\left(\mathbf{P} - \frac{\partial \psi}{\partial \mathbf{F}} \right)}_{\mathbf{P} = \frac{\partial \psi}{\partial \mathbf{F}}} \cdot \dot{\mathbf{F}} - \underbrace{\frac{\partial \psi}{\partial \rho}}_{:= Y} \dot{\rho} - \underbrace{\frac{\partial \psi}{\partial \delta}}_{:= \gamma} \dot{\delta} \geq 0 \quad (7)$$

In the considered case, the first Piola-Kirchhoff stress tensor is denoted by \mathbf{P} , and \mathbf{F} is the deformation gradient. The remaining dissipation inequality provides the thermodynamic conjugated forces of the model, which can be computed by $\frac{\partial \psi}{\partial \rho}$ and $\frac{\partial \psi}{\partial \delta}$, which are abbreviated to Y and γ , respectively. In order to define the onset of stiffness reduction as well as the hardening or softening behavior, the stiffness reduction criterion is defined as

$$\Phi = Y - Y_0 - \gamma(\delta) \leq 0 \quad (8)$$

Here, Y_0 is an additional material parameter and defines the threshold of stiffness reduction. According to the generalized normality rule, the evolution of stiffness reduction and hardening/softening variables are given by

$$\dot{\rho} = \dot{\kappa} \frac{\partial \Phi}{\partial Y} = \dot{\kappa}, \quad \dot{\delta} = -\dot{\kappa} \frac{\partial \Phi}{\partial \gamma} = \dot{\kappa} \quad (9)$$

where $\dot{\kappa}$ represents the required multiplier. Further, the Karush-Kuhn-Tucker-conditions must hold:

$$\dot{\kappa} \geq 0, \quad \Phi \leq 0, \quad \dot{\kappa} \Phi = 0 \quad (10)$$

The condition $\Phi = 0$ induce that thermodynamic driving force is generated whenever the stress is high enough and stiffness reduction is accumulating. On the contrary stiffness reduction does not evolve, for example in case of unloading, if $\Phi < 0$. Therefore, in this framework, stiffness reduction can only grow ($\dot{\kappa} \geq 0$).

4 Fitting procedure and selected experiments

The model contains fifteen parameters in total. The influence of the Lamé constant Λ in the second part of ψ_{el} can be neglected if the material is nearly incompressible and if $\Lambda \gg \mu_k(\rho)$ is adhered to for all k and ρ . In order to determine Λ in the correct order of magnitude, a computation based on the bulk modulus K from a compression test can be done separately at the beginning of the fitting procedure. For the computational determination of Λ , the compression modulus K was determined from the compression test in Fig. 4 with

$$K = \frac{p}{\frac{dV}{V}} = 1176 \text{ MPa} \quad (11)$$

With the Poisson's ratio ν , the following relationship between the Lamé constant Λ and the bulk modulus K applies from linear theory

$$\Lambda = \frac{3K}{1 + \frac{1}{\nu}} \quad (12)$$

With $\nu = 0.495$ one obtains $\Lambda = 1168$ MPa. This means that strictly speaking, the value only applies exactly to the linear initial range. To get one parameter set for a representation of all loading conditions, it is necessary to fit the remaining parameters simultaneously to results of a tension test and a shear test. Experiments to consider tension could be uniaxial or biaxial tension tests, and simple shear or pure shear experiments are both suitable for the consideration of shear tests. For the fitting procedure, the remaining parameters are initially divided into two groups. The first parameter group comprises the parameters μ_k^∞ and α_k , which describe the general S-shape of the stress-strain curve. The second group contains the parameters from the stiffness reduction (p_k), the control term (c_1, c_2) and the artificial parameters (μ_k^0). This group influences the occurrence and progression of stiffness reduction. These two groups can be fitted independently. The first group containing μ_k^∞ , which relates to the last unloading path, can be fitted together with α_k to the last stress-strain curve measured in the experiment and the remaining parameters (group 2) are fitted to the experimental results of the cyclically loaded tests, Fig. 5.

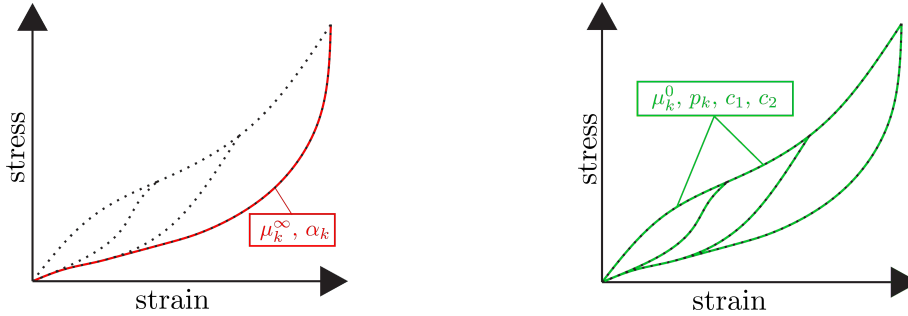


Fig. 5: Separate parameter fitting to last unloading path and to cyclic experimental data

The parameters were adjusted using the Optimization Toolbox™ in MATLAB, which enables a nonlinear algorithm for least squares, *lsqcurvefit*. For a simultaneous fit it is necessary to feed the test data into the algorithm in matrix form. The number of data points of all test data must correspond to each other. With manual weighting of the test data to achieve better fitting results, the matrix entries of different lengths can be filled by adding zero vectors. The fitted parameter set (Tab. 1) results in a very good representation of the uniaxial tension test and of a pure shear test, shown in Fig. 6.

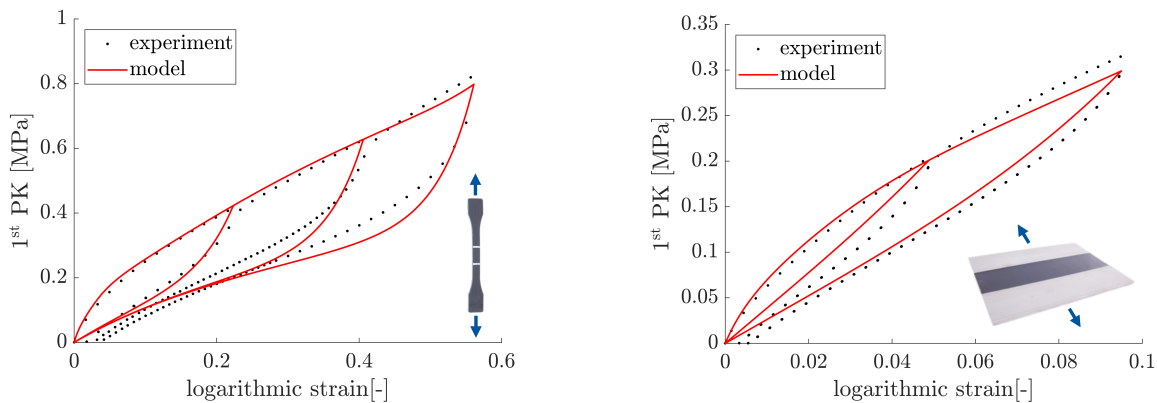


Fig. 6: Simultaneous fit to uniaxial tension test and pure shear test

Tab. 1: Model parameters of the proposed model

elastic parameters							
μ_1^∞ [MPa]	μ_2^∞ [MPa]	μ_3^∞ [MPa]	α_1 [-]	α_2 [-]	α_3 [-]	Λ [MPa]	
0.250	$3.91E-07$	-0.195	0.011	21.422	-4.398	1168	
stiffness reduction parameters							
μ_1^0 [MPa]	μ_2^0 [MPa]	μ_3^0 [MPa]	p_1 [-]	p_2 [-]	p_3 [-]	c_1 [MPa]	c_2 [-]
33.496	0.118	-0.523	4312.2	149.27	1017.6	3327.8	43.73

In general, the material parameters are determined to positive values. However, in order to map the S-shaped curve observed in the experiment, one exponent α_k must be negative as also shown by Ogden (1984). In Ogden (1972) the stability condition $\mu_k \alpha_k > 0$ is defined. From this, it follows that with a negative exponent α_k the corresponding μ_k must also be negative.

5 Model validation

To validate the model, its prediction regarding multiaxial stress states is compared with experimental data. For this, the model formulation was implemented as user material subroutine into the FEM software FEAP Taylor (2014). In addition to the possibility

of using the standard element $Q1$, the use and suitability of an advanced finite element technology was investigated, because modeling hyperelastic materials can evoke mesh distortion. The used element formulation, which is very efficient and robust against mesh distortion was formulated in Reese (2005). This formulation makes use of a reduced integration plus adaptive hourglass stabilization concept. The stabilization factors are computed based on the enhanced strain method. Moreover, this element formulation is very efficient from computational point of view, due to the integration in only one Gaussian point. For validation, two examples will be shown and discussed in the following. As a first example, a so called butt joint tensile test was chosen. This bonded specimen shows a large number of practice-relevant multi-axial stress states and is therefore particularly suitable for checking material laws. Two steel cylinders are connected to each other by an adhesive layer. The test was carried out under strain-control with cyclic loading. During loading the adhesive layer was elongated in axial direction. By using symmetry, the test specimen can be calculated two-dimensionally or three-dimensionally on a circular cylinder sector. The following results were generated with the displacement-controlled calculation of a circular cylinder sector whose cross-section is shown in Fig. 7. Based on the study of mesh convergence, shown in Fig. 8, 390 elements were chosen, because this mesh has already reached a converged solution. The model prediction compared to experimental results is shown in Fig. 9 and shows a very good match. For this computation the fitted parameters from Section 4 were used.

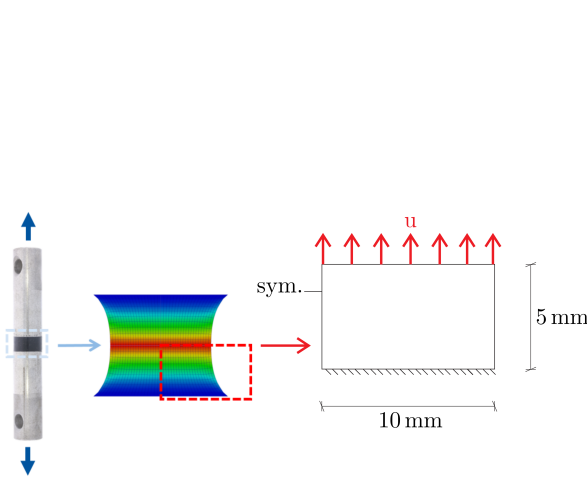


Fig. 7: Butt joint tensile test

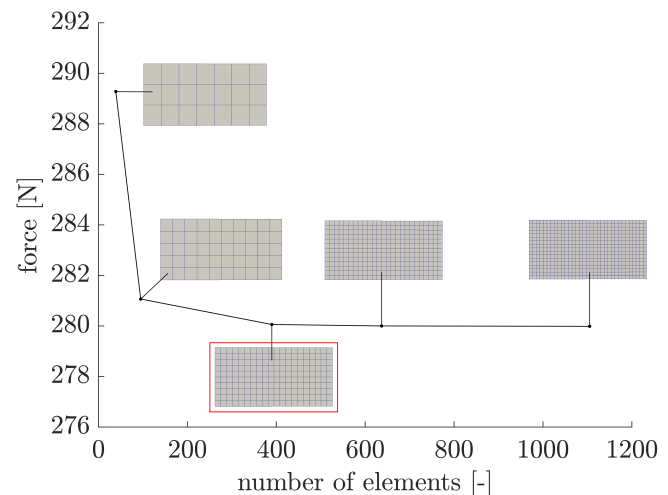


Fig. 8: Mesh convergence butt joint tensile test

A comparison of the advanced finite element formulation $Q1SP$ used here and the standard element $Q1$ of FEAP, in Fig. 10, shows that 390 elements with the standard element $Q1$ are obviously not sufficient to predict the experimental results well enough, whereas 390 elements with $Q1SP$ provide a reliable prediction. Also, increasing the number of elements to 1000 elements does not sufficiently improve the prediction using the $Q1$ elements. As already shown in the study of mesh convergence, about 1000 elements with $Q1SP$ lead to a similar prediction as 390 elements, these curves lie exactly on top of each other.

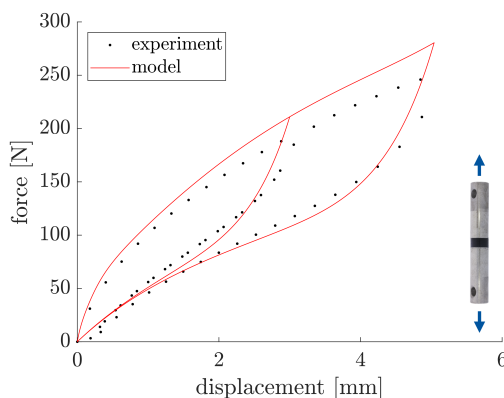


Fig. 9: Model prediction in comparison to experimental results for the butt joint tensile test

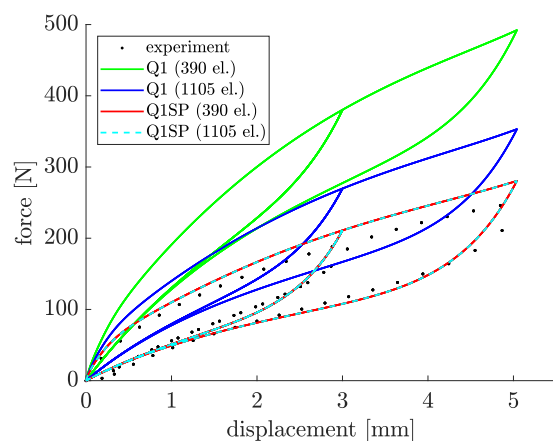


Fig. 10: Model prediction with different discretization and element types for the butt joint tensile test

The second example of validation is the specimen shown in Fig. 11, which is intended to resemble a component-like sample. With the aid of the component-like sample, a mixed stress state is to be generated within the connection. This results, for example, from a wind suction load on a façade element that is glued on all sides. Due to the plate loading of the glass pane, it undergoes a deflection which leads to a rotation in the joint.

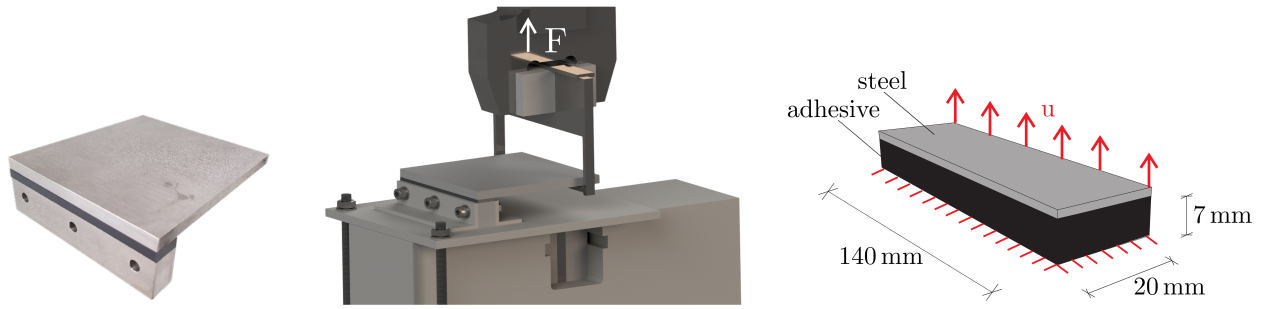


Fig. 11: Validation specimen in testing machine and simple sample for simulation

The specimen consists of a steel beam and a steel plate connected to each other by the adhesive layer. The lower steel beam is clamped in the test stand and at the end of the lever the sheet metal of the bonded specimen is pulled upwards in the load axis. For the simulation, the entire specimen was reduced to the sample section in Fig. 11, considering only the adhesive layer and a section of the upper steel plate. The bottom is completely fixed and the steel plate edge is moved upwards. The displacement applied to the lever end during the test was converted to the required displacement at the selected steel edge using the deflection angle for the displacement specification in the FE calculation. Since the evaluation of a force-displacement curve in this experiment is dependent on the length of the lever arm, the load-bearing behavior of the adhesive was represented in the form of a torsional momentum curve. As can be seen in Fig. 12, the length l_φ can be used to determine a momentum with $M = F \cdot l_\varphi$ that is independent of the length of the lever arm. The model prediction is in good match with the experimental results, see in Fig. 12. In particular, the maximum point from the prediction matches very well to the experimental data.

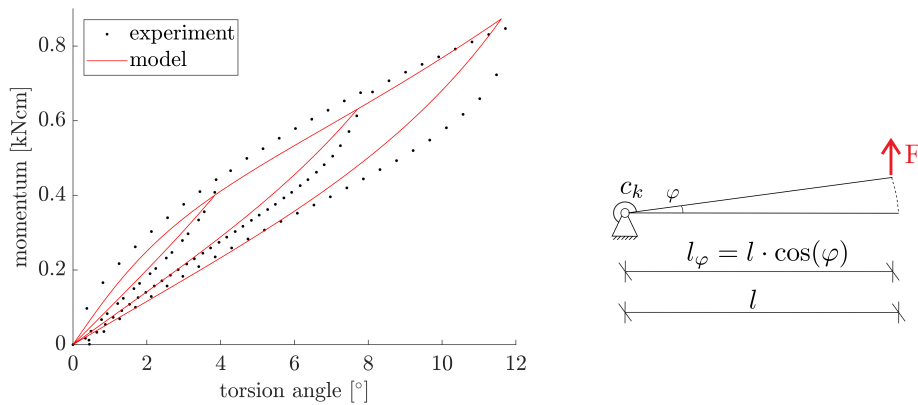


Fig. 12: Torsion angle and momentum relation

6 Comparison of the proposed model with the Ogden-Roxburgh model

To investigate the behavior of the proposed model in comparison to existing models from literature, the proposed model is also compared to the Ogden-Roxburgh model (Ogden and Roxburgh (1999)). First, the results of the simultaneous parameter fit to the uniaxial tension test and the pure shear test are compared, followed by the calculation of the butt joint tensile test, already shown in Section 5. The Ogden-Roxburgh model already implemented in the FE software Abaqus *Systèmes* (2016) was used for this comparison. The in Abaqus modified strain energy density function has the form

$$\psi(\bar{\lambda}_i, \eta) = \eta \psi_{dev}(\bar{\lambda}_i) + \Phi(\eta) + \psi_{vol}(J). \tag{13}$$

This function is splitted into a deviatoric part $\psi_{dev}(\bar{\lambda}_i)$ and a volumetric part $\psi_{vol}(J)$, depending on the deviatoric principal stretches $\bar{\lambda}_i = J^{-\frac{1}{3}} \lambda_i$ and the volume ratio J respectively. The continuous damage function $\Phi(\eta)$ depends on the damage variable η , which varies according to

$$\eta = 1 - \frac{1}{r} \operatorname{erf} \left(\frac{\psi_{dev}^m - \psi_{dev}}{m + \beta \psi_{dev}^m} \right), \tag{14}$$

where the Gauss error function $\operatorname{erf}(x)$ contains the ratio of ψ_{dev}^m , which is the maximum value of ψ_{dev} at a material point during

its deformation history. Corresponding to the Ogden model in Abaqus, $\psi_{dev}(\bar{\lambda}_i)$ is defined by

$$\psi_{dev}(\bar{\lambda}_i) = \sum_{i=1}^{N=3} \frac{2\mu_i}{\alpha_i^2} (\bar{\lambda}_1^{\alpha_i} + \bar{\lambda}_2^{\alpha_i} + \bar{\lambda}_3^{\alpha_i} - 3). \tag{15}$$

The volumetric part of the strain energy is defined by

$$\psi_{vol}(J) = \sum_{i=1}^{N=3} \frac{1}{D_i} (J - 1)^{2i}. \tag{16}$$

The corresponding elastic parameters μ_i , α_i , compression parameter D_i and the damage parameters r , β and m were determined in Abaqus itself on the basis of imported test data from the uniaxial tension test and the pure shear test (see Section 2) and are shown in Tab. 2.

Tab. 2: Model parameters of the Ogden-Roxburgh model

elastic parameters								
μ_1 [MPa]	μ_2 [MPa]	μ_3 [MPa]	α_1 [-]	α_2 [-]	α_3 [-]	D_1 [MPa ⁻¹]	D_2 [MPa ⁻¹]	D_3 [MPa ⁻¹]
-44.051	19.112	25.859	1.524	2.039	0.969	2.18E - 02	0.0	0.0
damage parameters								
r [MPa]	m [MPa]	β [MPa]						
1.248	3.01E - 02	1.038						

In contrast to the parameter limitation of the proposed model presented in Section 4, the parameters in Abaqus are controlled during the fit to the experimental data by checking the Drucker stability [Systèmes \(2016\)](#). A limitation of the parameters μ_i and α_i , as in the proposed model by $\mu_i \alpha_i > 0$, does not exist in Abaqus.

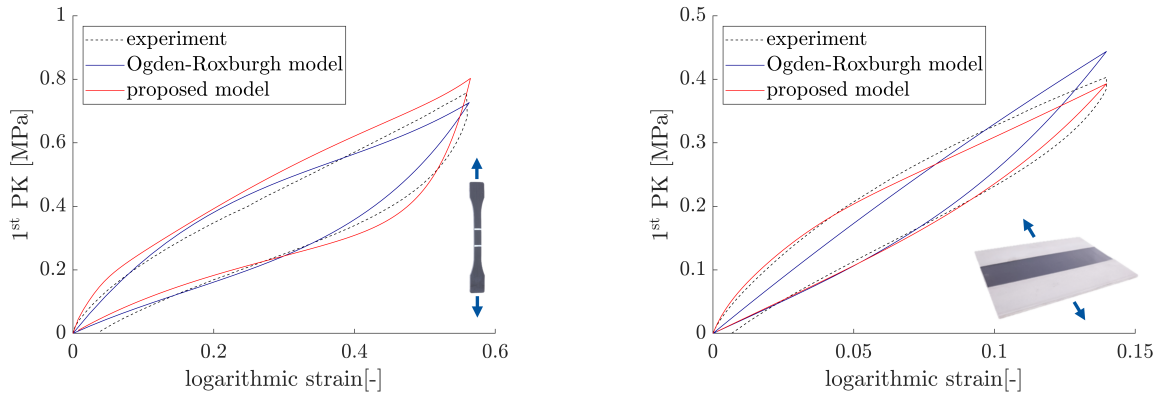


Fig. 13: Comparison of Ogden-Roxburgh model and proposed model in simultaneous fit to uniaxial tension test and pure shear test

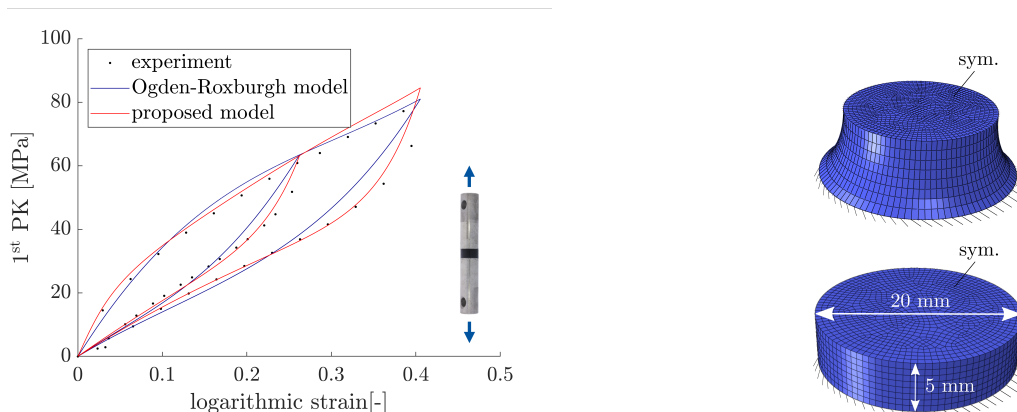


Fig. 14: Comparison of Ogden-Roxburgh model and proposed model in simulation of butt joint tensile test

The results fitted by the Ogden-Roxburgh model compared to the results fitted by the proposed model in Section 4 are shown in Fig. 13. A significantly better fitting result is provided by the proposed model for the unloading path in the uniaxial tension test compared to the Ogden-Roxburgh model. The pure shear test is described much better in the initial range by the proposed model and up to an elongation of 10% also in the relief range. The Ogden-Roxburgh model, on the other hand, strongly underestimates the initial range of the pure shear test and overestimates the actual material behavior at higher strains. The further investigation shows the comparison of the model responses for the calculation of the butt joint tensile test from Section 5. For this, the element C3D8RH was used in Abaqus. The stress-strain behavior of the sample with corresponding geometry from Fig. 7 is shown in Fig. 14. Similar to the comparison with the fits on the uniaxial tension test, the proposed model also matches the unloading paths better than the Ogden-Roxburgh model. On the other hand, the maximum stress is better predicted by the Ogden-Roxburgh model.

7 Conclusion and outlook

A flexible model for a hyperelastic material with exchangeable parts such as the stiffness reduction function, the elastic formulation, and the control term was presented. The parameters of the model were obtained from a staggered fitting procedure and were successfully fitted to compression test, uniaxial tensile, and pure shear test data simultaneously. First computational results demonstrated the accurate prediction of the proposed model, enabling the representation of multi-axial stress states of a hyperelastic material behavior considering stiffness reduction (Mullins effect) at large deformations. For the implementation in the FE program FEAP the element formulation Q1SP was used. It could be observed that compared to the standard element formulation Q1 for Q1SP a significantly smaller number of elements is required to achieve acceptable results. In a further step, the efficiency, parameter determination and the accuracy of the new model were compared with the Ogden-Roxburgh model from the literature and will also be compared with other models from the literature in future research work. In order to extend the proposed material model by a failure prediction, it would first be necessary to investigate the failure behavior within experimental studies. Based on these results, the model formulation can be extended to improve the prediction possibilities. Furthermore, the consideration of plastic deformation could be another step to make the model formulation more flexible and to achieve a higher agreement between the real material behavior and the model response.

Acknowledgments

Financial support of the the project RE 1057/46-1 by the German Science Federation (DFG) and the project IGF 19158 N by German Federation of Industrial Research Associations (AiF) is gratefully acknowledged.

References

- E. M. Arruda and P. A. Przybylo. An investigation into the three-dimensional stress-birefringence-strain relationship in elastomers. *Polymer Engineering and Science*, 35(5):395–402, 1995.
- M. F. Beatty and S. Krishnaswamy. The Mullins effect in equibiaxial deformation. *Zeitschrift für angewandte Mathematik und Physik ZAMP*, 51(6):984–1015, 2000.
- D. Besdo, J. Ihlemann, J. G. R. Kingston, and A. H. Muhr. Constitutive Models for rubber III. *Balkema*, page 309, 2003.
- M. Böl. *Numerische Simulation von Polymernetzwerken mit Hilfe der Finite-Elemente-Methode; Dissertation*. Number 135. Ruhr- Universität Bochum; Institut für Mechanik; Mitteilungen aus dem Institut für Mechanik Nr. 135, 2005.
- H. Bouasse and Z. Carrière. Courbes de traction du caoutchouc vulcanisé. *Annales de la Faculté des Sciences*, 5:257–283, 1903.
- T. Brepols, S. Wulfinghoff, and S. Reese. Gradient-extended two-surface damage-plasticity: micromorphic formulation and numerical aspects. *International Journal of Plasticity*, 97:64–106, 2017. doi: [10.1002/pamm.201610048](https://doi.org/10.1002/pamm.201610048).
- F. Bueche. Mullins effect and rubber-filler interaction. *Journal of Applied Polymer Science*, 5(15):271–281, 1961.
- S. Cantournet, R. Desmorat, and J. Besson. Mullins effect and cyclic stress softening of filled elastomers by internal sliding and friction thermodynamics model. *International Journal of Solids and Structures*, 46(11-12):2255–2264, 2009.
- J. Diani, B. Fayolle, and P. Gilormini. A review on the Mullins effect. *European Polymer Journal*, 45:601–612, 2009. doi: [10.1016/j.eurpolymj.2008.11.017](https://doi.org/10.1016/j.eurpolymj.2008.11.017).
- A. Dorfmann and R. W. Ogden. A constitutive model for the Mullins effect with permanent set in particle-reinforced rubber. *International Journal of Solids and Structures*, 41:1855–1878, 2004.
- ETAG. *ETAG no. 2. Guideline for European technical approval for structural sealant glazing kits.*, 2012.
- J. A. C. Harwood, L. Mullins, and A. R. Payne. Stress softening in natural rubber vulcanizates. Part II. Stress softening effects in pure gum and filler loaded rubbers. *Journal of Applied Polymer Science*, 9(9):3011–3021, 1965.
- J. Ihlemann. Richtungsabhängigkeiten beim Mullins-Effekt. *KGK Kautschuk Gummi Kunststoffe*, 58:438, 2005.
- M. Itskov, E. Haberstroh, A. E. Ehret, and M. C. Vöhringer. Experimental observation of the deformation induced anisotropy of the Mullins effect in rubber. *KGK Kautschuk Gummi Kunststoffe*, 59:93, 2006.
- M. A. Johnson and M. F. Beatty. The Mullins effect in uniaxial extension and its influence on the transverse vibration of a rubber string. *Continuum Mechanics and Thermodynamics*, 5(2):83–115, 1993.
- H. Kahraman, G. W. Weinhold, E. Haberstroh, and M. Itskov. Anisotroper Mullins-Effekt bei rußgefüllten Elastomeren. *KGK Kautschuk Gummi Kunststoffe*, 63(3):64–69, 2010.

- P. A. L. S. Martins, R. M. Natal Jorge, and A. J. M. Ferreira. A comparative study of several material models for prediction of hyperelastic properties: Application to silicone-rubber and soft tissues. *Strain*, 42:135–147, 2006.
- L. Meunier, G. Chagnon, D. Favier, L. Orgéas, and P. Vacher. Mechanical experimental characterisation and numerical modelling of an un-filled silicone rubber. *Polymer Testing*, 27:765–777, 2008.
- M. Mooney. A theory of large elastic deformation. *Journal of Applied Physics*, 11:582–592, 1940.
- L. Mullins. Effect of stretching on the properties of rubber. *Rubber Chemistry and Technology*, 21(2):281–300, 1948.
- R. W. Ogden. Large deformation isotropic elasticity—on the correlation of theory and experiment for incompressible rubberlike solids. *Proceedings of the Royal Society of London. Series A: Mathematical and Physical Sciences*, 326(1567):565–584, 1972.
- R. W. Ogden and D. G. Roxburgh. A pseudo-elastic model for the Mullins effect in filled rubber. *The Royal Society*, 455: 2861–2877, 1999.
- R.W. Ogden. *Non-linear elastic deformations*. Dover Publications, 1984.
- H. Pawelski, D. Besdo, R. H. Schuster, and J. Ihlemann. *Constitutive Models for Rubber II*, volume 27.
- Stefanie Reese. On a physically stabilized one point nite element formulation for three-dimensional nite elasto-plasticity. *Computer Methods in applied Mechanics and Engineering*, 194:4685–4715, 2005. doi: [10.1016/j.cma.2004.12.012](https://doi.org/10.1016/j.cma.2004.12.012).
- C. Richter, B. Abeln, A. Geßler, and M. Feldmann. Structural steel-glass facade panels with multi-side bonding - Nonlinear stress-strain behaviour under complex loading situations. *International Journal of Adhesion and Adhesives*, 55:28–28, 2014. URL <https://doi.org/10.1016/j.ijadhadh.2014.07.004>.
- R.S. Rivlin. Large elastic deformations of isotropic materials. IV. Further developments of the general theory. *Philosophical Transactions of the Royal Society London A: Mathematical, Physical and Engineering Sciences*, 241:379–397, 1948.
- J.-W. Simon, D. Höwer, B. Stier, S. Reese, and J. Fish. A regularized orthotropic continuum damage model for layered composites: intralaminar damage progression and delamination. *Computational Mechanics*, 60(3):445–463, 2017. doi: [10.1007/s00466-017-1416-1](https://doi.org/10.1007/s00466-017-1416-1).
- P. Steinmann, M. Hossain, and G. Possart. Hyperelastic models for rubber-like materials: consistent tangent operators and suitability for Treloar’s data. *Archive of Applied Mechanics*, 82(9):1183–1217, 2012. doi: [10.1007/s00419-012-0610-z](https://doi.org/10.1007/s00419-012-0610-z). URL <http://link.springer.com/article/10.1007/s00419-012-0610-z>.
- Dassault Systèmes. Abaqus, Release 6.16. 2016.
- R. L. Taylor. *FEAP - A finite element analysis program*, 2014.